Fermi surface nesting driven anomalous Hall effect in magnetically frustrated Mn_2PdIn

Afsar Ahmed,[1,*] Arnab Bhattacharya,[1] Prashant Singh,[2] Ajay Kumar,[2]
Tukai Singha,[3] Anis Biswas,[2,†] Yaroslav Mudryk,[2] and Indranil Das[3,‡]

[1] *CMP Division, Saha Institute of Nuclear Physics, A CI of Homi Bhabha National Institute, Kolkata, WB-700064, India*
[2] *Ames National Laboratory, U.S. Department of Energy, Iowa State University, Ames, IA 50011, USA*
[3] *CMP Division, Saha Institute of Nuclear Physics, A CI of Homi Bhabha National Institute, Kolkata, WB 700064, India*

arXiv:2505.02769v1 [cond-mat.mtrl-sci] 5 May 2025

Noncollinear magnets with near-zero net magnetization and nontrivial bulk electronic topology hold significant promise for spintronic applications, though their scarcity necessitates purposeful design strategies. In this work, we report a topologically nontrivial electronic structure in metallic Mn_2PdIn, which crystallizes in the inverse Heusler structure and exhibits a spin-glassy ground state with quenched magnetization. The system features Weyl-type band crossings near the Fermi level and reveals a novel interplay among momentum-space nesting, orbital hybridization, and spin-orbit coupling. Comprehensive transport measurements uncover a pronounced anomalous Hall effect (AHE) in Mn_2PdIn. The observed quadratic relationship between the longitudinal and anomalous Hall resistivities highlights the intrinsic Berry curvature contribution to AHE. These findings establish inverse Heusler alloys as compelling platforms for realizing noncollinear magnets that host Weyl-type semimetallic or metallic phases-combining suppressed magnetization with robust electronic transport-thereby offering a promising route toward their seamless integration into next-generation spintronic devices.

Noncollinear magnetic ordering such as skyrmions[1–5], merons[6,7], hedgehogs[8,9] and spin spirals[10–12], challenge the conventional dichotomy of parallel or anti-parallel spin arrangements in traditional ferromagnets and antiferromagnets. Such non-collinear spin arrangements can exhibit ferroic responses, like the spontaneous Hall effects, without significant net magnetization while mitigating the stray field issues typically associated with ferromagnets[12–14]. Notably, these magnets, including Weyl semimetal Mn_3Sn[15,16], exhibit anomaly in transverse resistivity (ρ_{xy}) originating in the nontrivial electronic states proximate to the Fermi level, where large intrinsic Berry curvature drives a substantial AHE. However, the fundamental understanding of such noncollinear magnets exhibiting near-zero net magnetic moment yet delivering a robust transport response driven by the nontrivial electronic topology remains in its infancy[17]. This gap largely stems from the scarcity of materials that combine noncollinear magnetic ordering with Weyl semimetallic/metallic (WSM) electronic states[6,18,19], underscoring the need to explore novel materials fostering this synergy with robust electrical transport signal of magnetism for seamless interfacing with electronic devices.

The emergence of Weyl fermions necessitates the breaking of either inversion ($\mathcal{P}$) or time-reversal ($\mathcal{T}$) symmetry and can lead to large intrinsic AHE. Building on these prerequisites, Mn-based inverse Heusler alloys (iHA), featuring inherently broken $\mathcal{P}$ and multiple inequivalent magnetic sublattices[20], have emerged as a compelling platform for concerned synergy. The antiferromagnetic exchange interaction between the tetrahedrally coordinated Mn atoms and their highly localized octahedral counterparts stabilizes a ferrimagnetic ordering with a small net magnetization[18,21–23]. Despite vanishing magnetization, the intrinsic magnetism mediated broken-$\mathcal{T}$ lifts the spin degeneracy of electronic bands, facilitating the formation of Weyl points. Meanwhile, the moderately broken $\mathcal{P}$, while preserving the topological nature of the Weyl points, shifts them in three-dimensional momentum space to different energy levels from the Fermi level, precluding the emergence of a nodal-line semimetal phase[24]. Notably, the $4d$-transition-element-based iHA holds distinct advantages of reduced anti-site disorder and enhanced spin-orbit coupling (SOC) effects over their $3d$ counterparts.

In this context, we present Mn_2PdIn, a ternary derivative of cubic spin-glassy alloy Mn_3In[25] with peculiar electronic band structure featuring clear Fermi surface nesting exhibits magnetically frustrated ground state and significant AHE through combined experimental and theoretical study. Employing systematic magnetometry investigation, we reveal a stabilization of spin cluster-glassy ground state with a spontaneous magnetization of 0.46 μ_B/f.u., following a ferrimagnetic/ferromagnetic-like ordering near room temperature. These results underscore Mn-based iHA as a unique platform for exploring the interplay of noncollinear magnetism and topological electronic states.

Polycrystalline samples of Mn_2PdIn were synthesized through a conventional arc-melting process using high-purity (99.9%) constituent elements in an argon (Ar) atmosphere. Following the initial synthesis, the samples underwent annealing at 800° C for one week within evacuated sealed quartz tubes to ensure better homogeneity. The crystallographic structure and phase purity of the samples were evaluated using X-ray diffraction (XRD) at room temperature, employing Cu-K_α radiation with

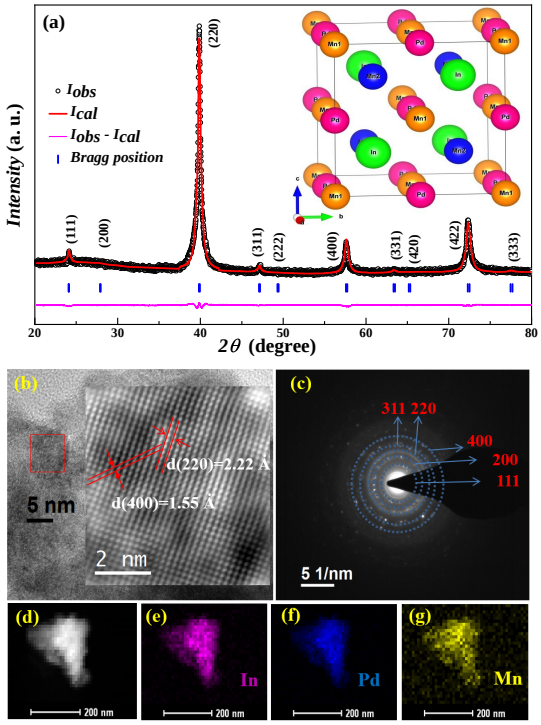

FIG. 1. (a) Rietveld refinement of room temperature XRD pattern of Mn_2PdIn. Inset shows crystal structure of the Mn_2PdIn compound. (b) High resolution TEM image, inset shows Fourier filtered image. (c) Selected-area electron diffraction (SAED) pattern. (d) STEM-HAADF image of the particle on which the elemental mapping was taken; elemental profile of (e) In (f) Pd and (g) Mn.

a Rigaku TTRX-III diffractometer. To verify the elemental composition and homogeneity of the samples, transmission electron microscopy (TEM) equipped with an energy-dispersive X-ray (EDX) spectrometer was utilized. The DC magnetic properties were investigated using a superconducting quantum interference device (SQUID-VSM) across a temperature range of 2 to 380 K and a magnetic field range of ± 7 T. The ac magnetic susceptibility measurements were conducted using an ac-equipped SQUID to provide further insight into the magnetic behavior of the samples. Magnetotransport properties were measured on samples with approximate dimensions of 4.50−4.60 mm (length), 2.00−2.05 mm (width), and 0.30−0.35 mm (thickness). These measurements were carried out using a 9T physical property measurement system (PPMS) in a standard four-probe arrangement, applying a DC current of 20 mA. Prior to the measurements, the ohmic nature of the current and voltage probe contacts, established with gold (Au) wires, was confirmed across the entire temperature range. For the assessment of field dependence of the resistivity at each temperature, the samples were cooled from room temperature to the desired measurement temperature in the absence of an applied magnetic field (H). The transverse resistivity (ρ_{xy}) was symmetrized using the relation, $\rho_{xy} = [\rho_{xy}(+H) - \rho_{xy}(-H)]/2$.

TABLE I. Table of crystallographic parameters, obtained from full Rietveld refinement analysis of room temperature XRD.

Lattice parameters: a = b = c = 6.399(5) $\AA$
Space group: F$\bar{4}$3m (No. 216)
R_f = 5.12, R_{Bragg} = 8.03, χ^2 = 1.67

Atomic Coordinates

Atom	Wyckoff position	x	y	z
Mn_{II}	4c	0.25	0.25	0.25
Pd	4d	0.75	0.75	0.75
Mn_I	4b	0.50	0.50	0.50
In	4a	0.00	0.00	0.00

Figure 1 (a) presents the Rietveld refinement of the room-temperature XRD pattern for Mn_2PdIn, obtained using a Rigaku TTRX-III diffractometer. The refinement confirms the inverse-Heusler alloy (iHA) structure [inset of Fig. 1 (a)] belonging to the cubic $F\bar{4}3m$ space group (216) with a lattice parameters a = 6.399(5) $\AA$, consistent with prior report[27]. The fitting parameters obtained from Rietveld refinement analysis are enlisted in Table I. This structure adheres to the stoichiometric arrangement of $XYX'Z$, with X, X', Y, and Z occupying 4c, 4d, 4b and 4a Wyckoff positions over four interpenetrating FCC sublattices. Notably, the absence of the (200) superlattice peak validates the iHA structure, consistent with the relative electronegativity of Mn and Pd[20]. Figure 1 (b) showcase high resolution TEM (HRTEM) image of Mn_2PdIn. The inset of Fig. 1(b) highlights the Fourier-filtered image of the specified region shown by the red box in the HRTEM image [Fig. 1(b)]. The interplanar spacings of 2.22 $\AA$ and 1.55 $\AA$ were identified as the [220] and [400] lattice planes, respectively. The polycrystalline nature of the compound is evident from the ring-shaped selected area electron diffraction (SAED) pattern, as shown in Fig. 1(c). The scanning TEM high-angle annular dark field (STEM-HAADF) image of the particle is presented in Fig. 1(d), on which elemental mapping and EDX analysis were performed. The elemental mapping of In, Pd, and Mn confirms the homogeneity of the compound, as shown in Fig. 1(e)-(g). Through XRD study, no impurity phase was detected which was further supported TEM-EDX elemental mapping.

Figure 2(a) depicts the DC-thermomagnetic curves, $M(T)$, measured under different applied fields (H) using zero-field-cooled (ZFC) and field-cooled (FC) protocols, showing an increase in M around room temperature, characteristics of a paramagnetic (PM) to ferromagnetic (FM)/ferrimagnetic (FiM)-like state, as reported earlier[27]. Notably, with lowering of temperature, a distinct bifurcation between M_{ZFC} and M_{FC} appears below the freezing temperature (T_F) ∼ 65.5 K. Remarkably,

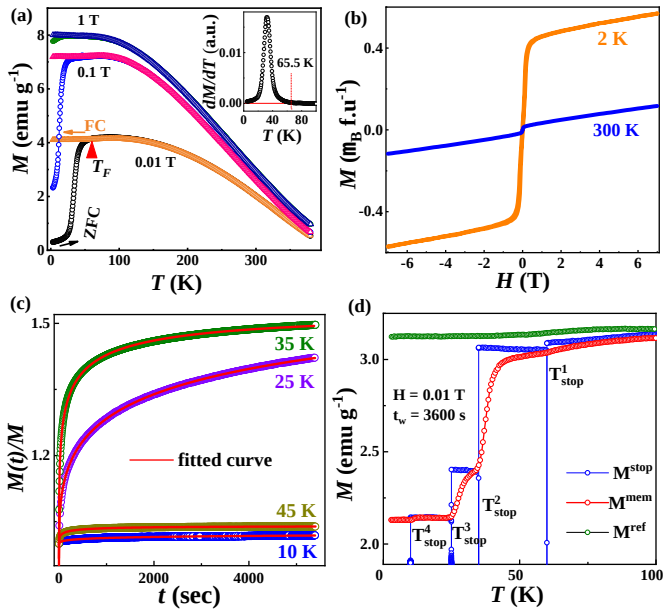

FIG. 2. (a) $M(T)$ curves under ZFC and FC protocols for various applied fields. Inset shows the derivative of 0.01 T ZFC $M(T)$ curve. (b) $M(H)$ curves at 2 and 300 K. (c) Time dependence of M for different T under $H = 0.01$ T. (d) Field-cooled-field stop memory curves.

the bifurcation is persistent under moderately high H of 0.1 T while T_F shifts towards lower temperature with increasing H, a behaviour typical for glassy phase[25,28,29,35].

The isothermal magnetization $M(H)$ at 2 K exhibits a soft FM/FiM-like behavior with negligible hysteresis, while the small spontaneous $M(H)$ at 300 K near $H = 0$ indicates a persistent FM/FiM contribution, consistent with earlier report[27] [Fig. 2(b)]. Even under a 7 T magnetic field at 2 K, the magnetization does not reach saturation but instead continues to exhibit field dependence, suggesting a tendency toward FiM behavior. However, it is worth mentioning that the derived saturation moment of 0.46 μ_B/f.u from the linear fitting of $M(H)$ curve in the 5 - 7 T range at 2 K, which is significantly lower than the expected value of 3 μ_B/f.u based on the Slatter-Puling rule ($M_{sat} = N_v - 24$; $N_v = 27$ is the total number of valence electron number), for a collinear FM ordering[31]. This deviation can be attributed to the presence of intersublattice antiferromagnetic correlation between two different Mn atoms located at the octagonally coordinated 4b site in the Mn-In sublattice and the tetragonal 4c site in the Mn-Pd plane, leading to a net FiM interaction[18,22,32,33]. The presence of competing interactions can lead to magnetic frustration and glassy magnetic state.

To get insights into the possible magnetic glassy state, we performed magnetic relaxation measurements at various temperatures under H of 10 mT, following ZFC from above T_F[34–36]. The time-dependent magnetization $M(t)$, shown in Fig. 2(c), reveals a gradual increase over time, a phenomenon characteristic of the magnetic aftereffect[35–39]. The curves are well-described by Kohlrausch-Williams-Watts equation: $M(t) = M_0(1 + aexp[-(t/\tau)^\beta])$, where M_0 is intrinsic magnetization, τ is characteristics relaxation time and β is shape parameter accounting for the energy barrier involved in the relaxation process. The extracted values of τ and β, listed in Table II, show that β remains in the range of 0.30 to 0.34 for all temperatures, consistent with the literature on SG systems[35–39]. Alongside magnetic relaxation, another notable aspect of the spin-glassy state is the manifestation of magnetic memory effects[25,36]. The FC memory effect was measured according to Sun *et al.*, where the sample is initially cooled down from room temperature to 2 K under H of 10 mT with intermediate temperature halts at T_{stop} (= 65, 35, 25 and 10 K) $< T_f$ for 1.5 hr while the field was switched off during each halting period. Following the lapse of t_w, the field was switched back on and the cooling was resumed while recording the temperature dependence of magnetization M^{stop} [Fig. 2(d)]. Following the cooling up to 2 K, the sample was heated to room temperature without any halts while recording M^{mem} and another conventional FC magnetization data was recorded as a reference (M^{ref}). The M^{mem} tries to retrace M^{stop} exhibiting anomalous bending at all T_{stop}, suggesting that the system remembers it previous history. This behaviour is consistent and resonates well with the literature of SG systems.

TABLE II. Fiting parameters t, β, τ for different temperatures using the Kohlrausch-Williams-Watts equation.

Temperature (K)	β	τ (s)
10	0.30(2)	2284
25	0.34(8)	3339
35	0.32(1)	229
45	0.33(4)	91

Following the DC-thermomagnetic observations, we investigated the $\chi_{ac}(T)$ under an excitation ac-field of 6 Oe for a broad frequency (f) range. Figure 3(a),(b) depicts the real (χ') and imaginary (χ'') part of $\chi_{ac}(T)$, respectively, for f ranging over three orders of magnitude. The $\chi'(T)$ showcase two distinct f-dependent positive peak-shift behavior at T_{1f} and T_{2f} [inset of Fig. 3(a)]. While T_{1f} does not manifest in DC measurements, T_{2f} resonates with T_F. Notably, $\chi''(T)$ exhibits frequency-dependent peaks at T_{1f} and T_{2f}, along with an f-independent peak around 250 K, indicating dissipative losses associated with successive SG transitions and domain formation, possibly following long-range magnetic ordering[40–42]. The anomaly at T_{1f} in $\chi'(T)$, which is absent in DC magnetometry, suggests the presence of nanoferromagnetic clusters. These clusters likely become suppressed or dissolve under the application of a small DC field (10 mT), possibly due to field-induced

alignment of magnetic moments or the reduction of spin fluctuations. For a conventional spin-glassy system, the relative shift of freezing temperature T_f per decade of f is expressed as[39], $\delta T_f = \Delta T_f/(T_f \Delta log f)$. In the present case, the estimated value of $\delta T_{1f} = 0.054$ and $\delta T_{2f} = 0.017$ lies typically in spin cluster-glass limit for both transitions[39]. For SG systems, the relaxation time $\tau(= f^{-1})$ at a particular T_f is related to the spin-spin correlation length ξ by a power-law divergence relation, $\tau = \tau_0 \left(\frac{T_f - T_g}{T_g}\right)^{-z\nu'}$, where τ_0 and T_g are the single spin-flip relaxation time and SG transition temperature for $f = 0$, respectively[39,43]. While $z\nu'$ is the dynamic critical exponent and ν' is the critical exponent of correlation length, $\xi = (T_f/T_g - 1)^{-\nu'}$. Typically, the $z\nu'$ lies between 4 to 12 for SG systems[44,45]. In Fig. 3(c), from our experimental results we obtain $z\nu' \simeq 11$ and $\tau_0 \simeq 10^{-8}$ for T_{1f} and $z\nu' \simeq 4$ and $\tau_0 \simeq 10^{-8}$ for T_{2f}, respectively. For both cases, τ_0 is a few orders higher than the value for canonical spin-glass ($\sim 10^{-12} - 10^{-13}$), suggesting a typical spin cluster-glass nature for the system[44]. To further verify the nature of the SG state, we analyzed the frequency dependence of T_f employing the Vogel-Fulcher relation, $\nu = \nu_0 exp\left(\frac{-E_a}{K_B(T_f - T_0)}\right)$, where ν_0, E_a, and T_0 are characteristic attempt frequency, activation energy and Vogel-Fulcher temperature, respectively[39,43]. The linearity relation of $1/\log(\nu_0/\nu)$ vs. T_f plot, depicted in Fig. 3(d), yields $E_a/K_B T_0 \simeq 2.12$ and 1.12 for T_{1f} and T_{2f}, respectively, affirming the cluster spin-glassy nature for Mn_2PdIn[39].

To understand ground state magnetic properties, we performed first principle electronic structure calculations for the samples . In this context, we employed density functional theory (DFT) method as implemented with Vienna Ab-initio Simulation Package (VASP) where the valence interaction among electrons was described by a projector augmented-wave (PAW) method[69,70] with an energy cutoff of 520 eV for the plane-wave orbitals. We used a $7\times7\times7$ ($11\times11\times11$) Monkhorst-Pack $k-$mesh for Brillouin zone sampling of cubic unit-cell during structural optimization (electronic-relaxation)[71]. A very high accuracy of total energy and force convergence, i.e., 10^{-8} eV/cell and 10^{-6} eV/Å, was set to get fully relaxed ionic-positions and electronic charges. We employ the Perdew-Burke-Ernzerhof (PBE) exchange-correlation functional in the generalized gradient approximation (GGA)[72]. In (semi)local functionals, such as GGA, the f-electrons are always delocalized due to their large self-interaction error[73,74].

Our calculations reveal that the ferri-magnetic (FiM) configuration is energetically preferred over the anti-ferromagnetic (AFM) or ferromagnetic (FM) state in Mn_2PdIn with a formation enthalpy of -67.95 meV/atom, resulting in a net magnetic moment of 0.39 μ_B per formula unit, which agrees quite well with experimentally obtained value from $M(H)$ curve. This arises from the opposing magnetic moments of 3.75 μ_B (Mn1) and -3.48 μ_B (Mn2), with small induced magnetic contributions

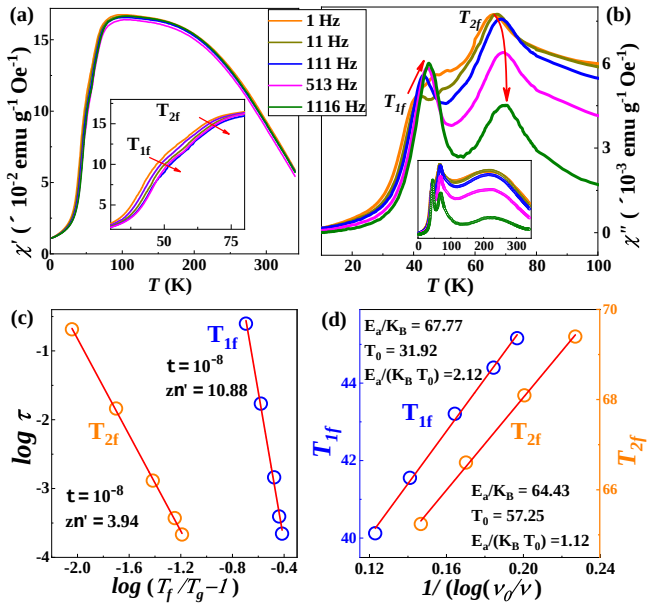

FIG. 3. (a),(b) Temperature variation of the real ($\chi'(T)$) and imaginary ($\chi''(T)$) components of ac-susceptibility for different f. Insets: (a) and (b) show an enlarged view of $\chi'(T)$ at low T and $\chi''(T)$ over 2 - 350 K, respectively. (c) f dependence of both freezing temperatures T_{f1} and T_{f2} where $\log\tau$ is plotted with $\log(T_f/T_g - 1)$. Red lines are the fitted curve using power law. (d) Frequency dependence for both the freezing temperatures plotted as T_{1f} and T_{2f} vs. $1/\log(\nu_0/\nu)$. Red lines are fitted curves.

from Pd (0.057 μ_B) and In (0.018 μ_B). Based on competing energetic FiM and FM, a mean-field approach which emphasizes spin-spin pair correlations is used to calculate the freezing temperature T_F of metallic spin glasses[75–78]. We used the relationship:

$$T_F = \frac{1}{k_B N} \sum_{i,j} \sqrt{J^2_{i,j,\text{avg}}}$$

to approximate the spin-glass temperature, where $J^2_{i,j,\text{avg}}$ is the average effective indirect exchange coupling over all possible configurations of magnetic ions and nonmagnetic ions, N is the total number of spins, and k_B is Boltzmann's constant[75]. The resulting estimate using DFT calculated J[FiM-AFM] $= -0.04295$ eV, eight spin centers ($N = 8$) in the unit-cell, and k_B (8.617 $\times10^{-5}$ eV·K^{-1}) was found to be 62.3 K, which is in good agreement with the experimentally observed $T_F = 65.5$ K [see Fig. 2(a)].

The band structure in Fig. 4(a) shows multiple moderately dispersive bands crossing the Fermi level (E_{Fermi}), particularly along high-symmetry lines such as $\Gamma \rightarrow X$. Around the Γ point, an electron-like parabolic band sits just above E_{Fermi}, characterized primarily by Mn e_g orbital weight. In contrast, near the L point, a flatter hole-like band dips just below E_{Fermi}, with strong contributions from Mn t_{2g} and Pd d-orbitals. This energy-

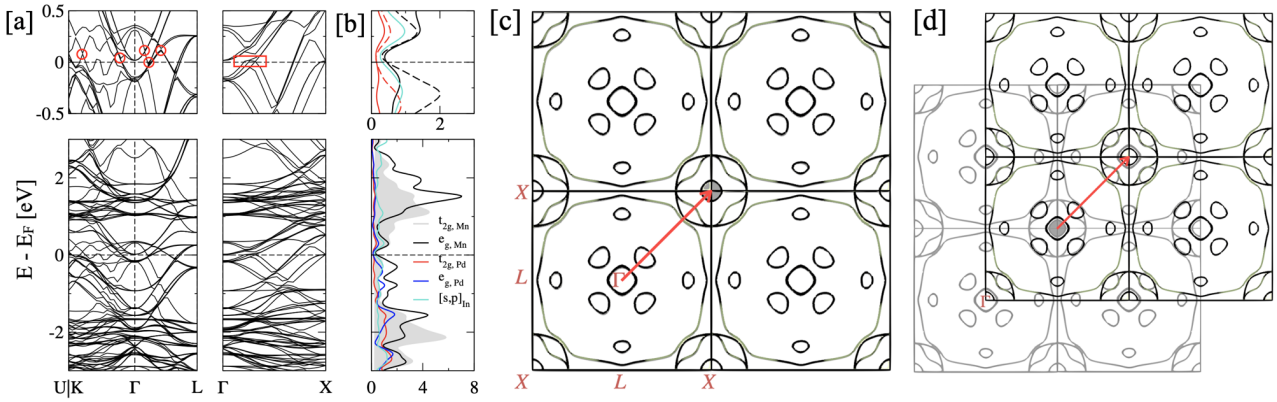

FIG. 4. (a, b) Electronic band structure and atom- and orbital-resolved density of states (DOS) for Mn_2PdIn including spin-orbit coupling (SOC). The band structure reveals multiple band crossings near the Fermi level, with an electron-like Mn e_g band at Γ and flatter, hole-like bands near L and X exhibiting significant Pd t_{2g} and Mn t_{2g} character, creating quasi-nested Fermi surface segments. The projected DOS confirms dominant Mn e_g contributions at the Fermi level, alongside hybridization with Pd d- and In $\{s, p\}$-states, which enhances inter-orbital scattering pathways. Fermi surface contours of Mn_2PdIn with SOC illustrating nesting-driven interband scattering, where (c) the red arrow highlights a prominent nesting vector connecting electron-like pockets at the Γ point with hole-like pockets near the X point in the $k_x - k_y$ plane, and (d) superimposed Brillouin zones emphasize the commensurate nature of the Γ-X nesting arising from Mn e_g-derived conduction bands overlapping with flat, hybridized valence bands near X, thereby facilitating momentum-dependent scattering linked to the anomalous Hall effect.

momentum configuration establishes a nesting condition across the Brillouin zone via a vector $\boldsymbol{q}_{\text{nest}} \sim \Gamma \to X$, which connects parallel Fermi surface contours separated by approximately 0.5 - 0.7 Å^{-1} in reciprocal space. These features create quasi-parallel energy contours, enhancing the nesting susceptibility between the Γ and L points. Moreover, in systems like Mn_2PdIn, which break time-reversal symmetry due to magnetic ordering, such crossings are strong candidates for Weyl points, especially in the presence of spin-orbit coupling (SOC). The SOC in this system, introduced primarily by the Pd atoms, acts to lift degeneracies and generate small energy gaps (on the order of 20−50 meV). The presence of these band crossings in close proximity to the Fermi level is crucial for stabilizing symmetry-protected Weyl nodes, which may serve as localized sources and sinks of Berry curvature, thereby contributing significant intrinsic AHC. The red-boxed region along the Γ → X and Γ → K points highlights another important feature: the presence of quasi-flat bands that span the Brillouin zone. These bands exhibit low group velocities, resulting in an enhanced density of states near the Fermi level. From a transport standpoint, flat bands in close energetic alignment with linearly dispersing Weyl-like bands can amplify the magnitude of Berry curvature due to enhanced dwell time of quasiparticles and increased interband coherence. The strong orbital selectivity of these bands, with dominant Mn e_g and Pd t_{2g} contributions as shown in Fig. 4(b), facilitates large matrix elements for anomalous velocity transitions. Notably, in Fig. 4(b), the PDOS confirms that the states at the Fermi level are dominated by Mn e_g orbitals, with a sharp DOS peak indicating a high electronic density and associated susceptibility to magnetic and transport instabilities.

The flatter bands from Γ → X display increased hybridization from Pd t_{2g} and e_g states, whose symmetry and localization promote band anticrossings. In contributions are visible through weakly dispersive $\{s, p\}$-states that mediate broader hybridization across the valence manifold. The resulting orbital entanglement near E_{Fermi} leads to multiple avoided crossings, especially along Γ → L, as observed in the band structure- a hallmark of SOC-induced band distortion. The combined proximity of Weyl-like crossings and flat bands near E_{Fermi}, together with orbital hybridization and spin-orbit splitting, may enable a large momentum-resolved asymmetry in electronic velocity. Quantitatively, the electronic structure of Mn_2PdIn supports the possibility of a robust intrinsic anomalous Hall effect.

This electronic complexity culminates in the Fermi surface shown in Fig. 4(c) & (d), where nested electron- and hole-like pockets emerge around the Γ and X points, respectively. The red arrow traces a well-defined nesting vector $\boldsymbol{q}$, enabling low-energy electronic transitions between states of opposite curvature and group velocity. These transitions are allowed because of the energetic closeness (within ±0.2 eV) and similar orbital symmetry, with the pockets forming nearly commensurate contours repeated across Brillouin zones due to the cubic symmetry of the system. The SOC, introduced via the heavy Pd and In atoms, further lifts degeneracies near band crossings, producing small but finite gaps where previously degenerate states are now separated by orbital mixing. This splitting introduces directional asymmetry in the velocity matrix elements $\langle u_{n\boldsymbol{k}} | v_x | u_{m\boldsymbol{k}} \rangle$, where n, m index the nested bands. These asymmetries generate

a momentum-resolved imbalance in carrier distribution under an external electric field, producing a finite transverse conductivity σ_{xy}. Importantly, the proximity of the Mn e_g-dominated conduction band to quasi-flat valence bands at X not only amplifies the density of interband states but also increases the phase space for asymmetric scattering. The nesting vector $\boldsymbol{q}_{\rm nest} \sim \Gamma \rightarrow X$ bridges bands with strong orbital contrast (Mn $e_g \leftrightarrow$ Pd t_{2g}), enabling scattering pathways that break inversion symmetry locally in momentum space.

We anticipate significant AHE in Mn_2PdIn as a natural outcome of the combined effects of Fermi-surface nesting, SOC-induced band hybridization, and orbital anisotropy. The alignment of electron-like bands at Γ with quasi-flat hole-like bands near X, their orbital composition (especially Mn e_g and Pd t_{2g}), and the scattering permitted by these nesting vectors all drive momentum-dependent asymmetric conduction. To further confirm role of electronic-structure, we evaluated intrinsic AHE ($\sigma^A_{xy,\rm int}$) of Mn_2PdIn using the Kubo formalism, as outlined by Yao *et al.* and others[79–81]. The imaginary part of the off-diagonal elements of the optical conductivity is first computed, followed by the determination of the real part through a Kramers-Kronig transformation. This approach, based on linear response theory, relates the AHC to the electronic structure by integrating the velocity operators and wavefunctions over the Brillouin zone. The intrinsic AHC corresponds to the static limit of the off-diagonal optical conductivity, i.e., $\sigma^1_{xy,\rm int}(\omega = 0)$. Alternatively, AHC can also be obtained by integrating the Berry curvature over the Brillouin zone, an approach that has been shown to yield numerically equivalent results[82].[82]. To ensure accuracy, we employed a dense k-point mesh for AHC calculations. Multiple fine k-point meshes were used, with the densest being $70\times70\times70$ in $F4\bar{3}m$ Brillouin zone. The AHC was fitted to a polynomial to obtain the converged theoretical value, i.e., the extrapolated value at dense $k-$mesh, following the approach in Ref.[80].

Notably, electronic-structure in Fig. 4 reveals that bands near the Fermi level consist of highly dispersive Mn$-d$, Pd$-d$, and In$-p$ hybridized bands with very low electronic density. As a result, the intrinsic AHC, as obtained from DFT combined with Kubo formalism, is not very large, measuring approximately 132 S cm^{-1}. However, when the energy is reduced (increased) to -2.1 (0.8 eV), $\sigma^A_{xy,int}$ increases dramatically to about 937 S cm^{-1} ($\sim$1003 S cm^{-1}). The enhanced AHC is primarily attributed to the increased electronic DOS in these energy regions, leading to stronger contributions. The calculated AHC variation with energy suggests strong sensitivity to the chemical potential, highlighting the need for precise control over doping or external Fermi level shifts. Such behavior is consistent with trends observed in other Heusler compounds, where the AHC is strongly dependent on the band structure and the degree of hybridization between transition metal d$-$states. For instance, in Co_2MnAl and Co_2MnSi, the AHC has been reported to be around 500 S cm^{-1} and 1500 S cm^{-1}[81,85], respectively, with the variation attributed to the different band dispersions near the Fermi level and the presence of gapped or nodal structures in the spin-polarized bands[86]. In comparison, the AHC in Mn_2CoAl, a compensated ferrimagnetic Heusler compound, reaches values as high as 1500-2000 S cm^{-1} due to the presence of Weyl-like band crossings and enhanced Berry curvature contributions[83]. Similar trends have been observed in Fe-based Heusler compounds, such as Fe_2CrSi and Fe_2MnGa, where the interplay of band topology plays a crucial role in determining the magnitude of AHC[87]. Compared to these materials, Mn_2PdIn exhibits an intrinsic AHC due to the lower density of hybridized Mn$-d$, Pd$-d$, and In$-\{s,p\}$ states at the Fermi level. However, the significant increase in AHC when shifting the energy away from Fermi level suggests that this compound may host other extreme of anomalous AHC (very high) values under strain or doping induced modifications of the band structure. The observed energy dependence of AHC highlights the crucial role of band filling effects and suggests possible routes to enhance the AHC in similar compounds through controlled electronic structure engineering. The intriguing electronic structure and theoretical predictions motivate us to perform detailed transport and magneto-transport measurements on the sample.

As shown in Fig. 5(a), zero-field ρ_{xx} exhibits a metallic nature with a residual resistivity ratio ($\rho_{300\rm K}/\rho_{2\rm K}$) of 1.36, consistent with the characteristics of Heusler alloys[18,46,47]. To investigate the principal scattering mechanism governing ρ_{xx}, we fit $\rho_{xx}(T)$ below T_f, employing the e-e scattering T^2 dependence. However, a better fit is obtained on the incorporation of the spin-fluctuation $T^{3/2}$ term, resulting $\rho_{xx} = \rho_0 + aT^2 + bT^{3/2}$, where ρ_0 are residual resistivity and a, b are constants[47,48]. The fitting yields $\rho_0 = 118.26$ $\mu\Omega$ cm, $a = 1.28 \times 10^{-2}$ $\mu\Omega$ cm K$^{-3/2}$ and $b = 7.04 \times 10^{-4}$ $\mu\Omega$ cm K^{-2}, suggest a dominant spin-fluctuation contribution at low temperatures. This underscores a strong electron-magnon interaction between the localized moments and conduction electrons, consistent with the glassy nature of the magnetic ordering[48].

Now we focus on the Hall transport data. Figure 5(c) depicts the $\rho_{xy}(H)$ isotherms at various T. Notably, alongside Lorentz force-mediated normal Hall resistivity ρ^O_{xy}, an additional component mirroring $M(H)$ appears in ρ_{xy}, in sharp contrast to parent SG Mn_3In[25]. This observation, coupled with the minuscule magnetoresistance [Fig. 5(b)], suggest a dominant AHC contribution in ρ_{xy}. For a FM/FiM system, ρ_{xy} is expressed as, $\rho_{xy} = \rho^O_{xy} + \rho^A_{xy} = R_0H + R_SM$, where R_0, R_S are normal and anomalous Hall coefficients, respectively[49,50,88]. A linear fit of ρ_{xy} in the high-field range ($H = 5$ -7 T) yields ρ^A_{xy} and the slope R_0, as shown in the inset of Fig. 5(c). The negative slope of $\rho_{xy}(H)$ establishes electrons as the majority charge carriers, with a density of $\sim 10^{22}$ cm^{-3} at $T = 5$ K. Figure 5(d) illustrates the non-monotonic variation of ρ^A_{xy}, obtained from high field extrapolation

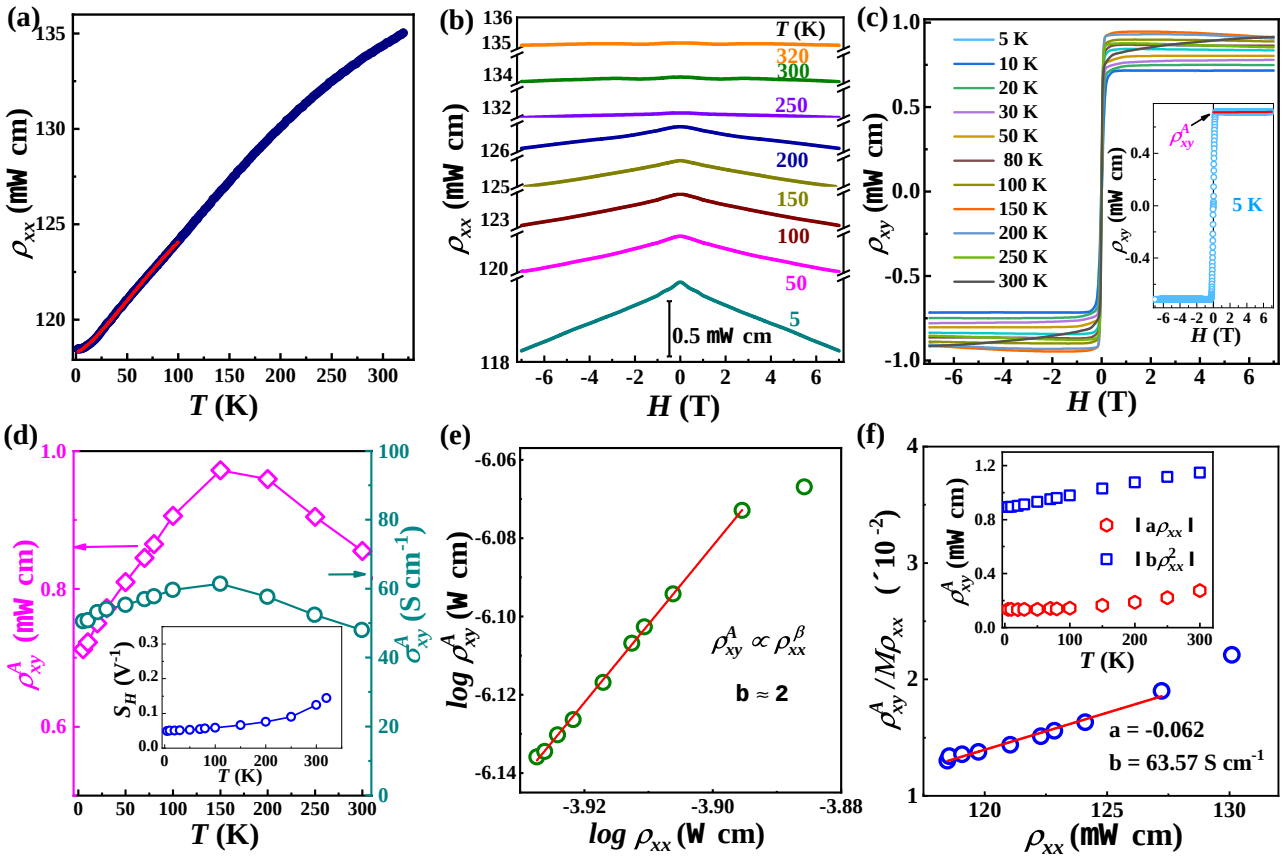

FIG. 5. (a) $\rho_{xx}(T)$ in zero field. Red line is the fitted curve (b) $\rho_{xx}(H)$ isotherms for various T. (c) Transverse resistivity for different T. Inset shows a linear fit of ρ_{xy} in the high-field range (H = 5 - 7 T), yielding ρ^A_{xy}. (d) Variation of ρ^A_{xy} and σ^A_{xy} with T. Insets show the T variation of scale factor S_H. (e) Power-law scaling of ρ^A_{xy} with ρ_{xx}. (f) TYJ scaling. Inset shows the T variation of *int*, *sj* and skew scattering component of AHC.

of ρ_{xy} isotherms, showcasing a linear increase up to 150 K followed by a decrease with increasing temperature. Despite this temperature dependence, the AHC obtained by the tensorial relation $\sigma^A_{xy} \approx \rho^A_{xy}/\rho^2_{xx}$, exhibits a T insensitive behaviour with $\sigma^A_{xy} \sim 50$ S cm^{-1} at $T = 5$ K. Accounting in the various mechanisms governing AHC, ρ^A_{xy} scales differently with ρ_{xx} and the observed quadratic relation, in Fig. 5(e), attests to the intrinsic (*int*) and/ or extrinsic side-jump (*sj*) rooted origin of AHC. Furthermore, the temperature independence of the anomalous Hall factor, $S_H = \sigma^A_{xy}/M$ [inset of Fig. 5(d)], aligns well with the Karplus-Luttinger theory, reinforcing its validity in describing the observed AHC[51].

To quantify the individual contributions, we adopt the *TYJ*-scaling relations for ρ^A_{xy}, *i.e.*, $\rho^A_{xy}/M\rho_{xx} = a + b\rho_{xx}$. Here, a is the skew-scattering coefficient and b relates to the intrinsic AHC[52,53]. The expected linear relation (for $\rho_{xx} \leq 127$ $\mu\Omega$ cm), as in Fig. 5(f), yields $a \approx$ -0.062 and $b \approx 63$ S cm^{-1}. The deviation from linearity for $T > 120$ K originates from the temperature dependence of M. Using these coefficients, we calculated the skew scattering term (aρ_{xx}) and the combined *int* and *sj* contribution (bρ^2_{xx}), plotting their temperature variations [inset of Fig. 5(f)]. This reveals that the contributions of *int* and *sj* mechanisms dominate the AHC across the investigated temperature range. At low temperatures, the reduced phonon scattering entangles σ^A_{sj} and $\sigma^A_{xy,int}$, present a challenge for quantification without an existing scaling framework. However, the estimated order of magnitude of σ^A_{sj} is significantly smaller than $\sigma^A_{xy,int}$, affirming the intrinsic nature of AHC in Mn_2PdIn.

We found that the experimentally obtained AHC for the sample is lower than that DFT calculated AHC (0 K). This discrepancy can likely be attributed to the polycrystalline nature of the sample, defects and/or finite-temperature effects, which are known to significantly reduce AHC by 50-80% compared to theoretical predictions[83,84]. The calculated AHC variation with energy suggests strong sensitivity to the chemical potential, highlighting the need for precise control over doping or external Fermi level shifts.

In conclusion, Mn_2PdIn, an inverse Heusler alloy, exhibits two distinct spin-glassy phases within a nearly compensated ferrimagnetic background, along with a no-

tably large intrinsic anomalous Hall conductivity. These characteristics position it as a promising candidate for spintronic applications, offering both quenched magnetization and robust topological transport properties. The quadratic scaling of anomalous Hall resistivity with longitudinal resistivity confirms the intrinsic origin of the anomalous Hall conductivity in this compound. Ab initio calculations reveal Weyl-type band crossings near the Fermi level, attributed to the breaking of time-reversal ($\mathcal{T}$) symmetry, thereby validating its topologically non-trivial electronic structure. We propose that the anomalous Hall effect in Mn_2PdIn is deeply rooted in the material's band topology and pronounced Fermi surface nesting. Our findings present a predictive criterion-nesting-induced inter-orbital scattering in spin-orbit-coupled systems-for identifying new anomalous Hall effect-active intermetallic compounds with Heusler and related crystal structures.

Works, performed at the Ames National Laboratory was supported by the Division of Materials Science and Engineering of the Office of Basic Energy Sciences, Office of Science of the U.S. Department of Energy (D.O.E). Ames National Laboratory is operated for the U.S. DOE by Iowa State University of Science and Technology under Contract No. DE-AC02-07CH11358. A.A. and A.B. would like to acknowledge SINP, India, and the Department of Atomic Energy (DAE), India for their fellowship. We acknowledge Mohammad Rezwan Habib and Prof. Indra Dasgupta from the School of Physical Sciences, Indian Association for the Cultivation of Science, Kolkata, for the initial theoretical assessment and fruitful discussions.

---

* afsar.ahmed@saha.ac.in
† anis@ameslab.gov
‡ indranil.das@saha.ac.in

[1] A. Fert, N. Reyren, and V. Cros, Magnetic skyrmions: advances in physics and potential applications, Nat. Rev. Mater. **2**, 17031 (2017).
[2] Y. Tokura and N. Kanazawa, Magnetic skyrmion materials, Chem. Rev. **121**, 2857 (2021).
[3] A. Fert, V. Cros, and J. Sampaio, Skyrmions on the track, Nat. Nanotechnol. **8**, 152 (2013).
[4] J. C. Gallagher, M. D. Stern, Y. Li, T. Liu, H. Zhang, W. Jin, J. L. Zhang, J.-H. Park, and R. He, Robust zero-field skyrmion formation in FeGe epitaxial thin films, Phys. Rev. Lett. **118**, 027201 (2017).
[5] R. Ozawa, S. Hayami, and Y. Motome, Zero-field skyrmions with a high topological number in itinerant magnets, Phys. Rev. Lett. **118**, 147205 (2017).
[6] P. Puphal, V. Pomjakushin, N. Kanazawa, V. Ukleev, D. J. Gawryluk, J. Ma, M. Naamneh, N. C. Plumb, L. Keller, R. Cubitt, et al., Topological magnetic phase in the candidate Weyl semimetal CeAlGe, Phys. Rev. Lett. **124**, 017202 (2020).
[7] X. Z. Yu, W. Koshibae, Y. Tokunaga, K. Shibata, Y. Taguchi, N. Nagaosa, and Y. Tokura, Transformation between meron and skyrmion topological spin textures in a chiral magnet, Nature **564**, 95–98 (2018).
[8] Y. Fujishiro, N. Kanazawa, T. Nakajima, X. Z. Yu, K. Ohishi, Y. Kawamura, K. Kakurai, T. Arima, H. Mitamura, A. Miyake, et al., Topological transitions among skyrmion-and hedgehog-lattice states in cubic chiral magnets, Nat. Commun. **10**, 1059 (2019).
[9] J. Zou, S. Zhang, and Y. Tserkovnyak, Topological transport of deconfined hedgehogs in magnets, Phys. Rev. Lett. **125**, 267201 (2020).
[10] S.-H. Yang, R. Naaman, Y. Paltiel, and S. S. P. Parkin, Chiral spintronics, Nat. Rev. Phys. **3**, 328–343 (2021).
[11] P. Park, W. Cho, C. Kim, Y. An, Y.-G. Kang, M. Avdeev, R. Sibille, K. Iida, R. Kajimoto, K. H. Lee, et al., Tetrahedral triple-Q magnetic ordering and large spontaneous Hall conductivity in the metallic triangular antiferromagnet $Co_{1/3}TaS_2$, Nat. Commun. **14**, 8346 (2023).
[12] N. J. Ghimire, A. S. Botana, J. S. Jiang, J. Zhang, Y.-S. Chen, and J. F. Mitchell, Large anomalous Hall effect in the chiral-lattice antiferromagnet $CoNb_3S_6$, Nat. Commun. **9**, 3280 (2018).
[13] T. Suzuki, R. Chisnell, A. Devarakonda, Y.-T. Liu, W. Feng, D. Xiao, J. W. Lynn, and J. G. Checkelsky, Large anomalous Hall effect in a half-Heusler antiferromagnet, Nat. Phys. **12**, 1119–1123 (2016).
[14] C. Shekhar, N. Kumar, V. Grinenko, S. Singh, R. Sarkar, H. Luetkens, S.-C. Wu, Y. Zhang, A. C. Komarek, E. Kampert, et al., Anomalous Hall effect in Weyl semimetal half-Heusler compounds RPtBi (R = Gd and Nd), Proc. Natl. Acad. Sci. USA **115**, 9140–9144 (2018).
[15] S. Nakatsuji, N. Kiyohara, and T. Higo, Large anomalous Hall effect in a non-collinear antiferromagnet at room temperature, Nature **527**, 212–215 (2015).
[16] X. Li, J. Koo, Z. Zhu, K. Behnia, and B. Yan, Field-linear anomalous Hall effect and Berry curvature induced by spin chirality in the kagome antiferromagnet Mn_3Sn, Nature Commun. **14**, 1642 (2023).
[17] L. Šmejkal, T. Jungwirth, and J. Sinova, Route towards Dirac and Weyl antiferromagnetic spintronics, Phys. Status Solidi (RRL) **11**, 1700044 (2017).
[18] A. Bhattacharya, M. R. Habib, A. Ahmed, B. Satpati, S. DuttaGupta, I. Dasgupta, and I. Das, Spin-valve-like magnetoresistance and anomalous Hall effect in magnetic Weyl metal Mn_2PdSn, Phys. Rev. B **110**, 014417 (2024).
[19] A. Ahmed, J. Sharma, A. Bhattacharya, A. Biswas, T. Singha, Y. Mudryk, A. Alam, and I. Das, Unconventional anomalous Hall effect in hexagonal polar magnet $Y_3Co_8Sn_4$, arXiv preprint arXiv:2502.03452 (2025).
[20] T. Graf, C. Felser, and S. P. Parkin, Simple rules for the understanding of Heusler compounds, Prog. Solid State Chem. **39**, 1–50 (2011).
[21] W. Shi, L. Muechler, K. Manna, Y. Zhang, K. Koepernik, R. Car, J. Van Den Brink, C. Felser, and Y. Sun, Prediction of a magnetic Weyl semimetal without spin-orbit coupling and strong anomalous Hall effect in the Heusler compensated ferrimagnet Ti_2MnAl, Phys. Rev. B **97**, 060406 (2018).
[22] J. Winterlik, G. H. Fecher, B. Balke, T. Graf, V. Alijani, V. Ksenofontov, C. A. Jenkins, O. Meshcheriakova, C. Felser, G. Liu, S. Ueda, K. Kobayashi, T. Nakamura, and

M. Wójcik, Electronic, magnetic, and structural properties of the ferrimagnet Mn_2CoSn, Phys. Rev. B **83**, 174448 (2011).

[23] R. Stinshoff, A. K. Nayak, G. H. Fecher, B. Balke, S. Ouardi, Y. Skourski, T. Nakamura, and C. Felser, Completely compensated ferrimagnetism and sublattice spin crossing in the half-metallic Heusler compound $Mn_{1.5}FeV_{0.5}Al$, Phys. Rev. B **95**, 060410 (2017).

[24] A. A. Zyuzin, S. Wu, and A. A. Burkov, Weyl semimetal with broken time reversal and inversion symmetries, Phys. Rev. B **85**, 165110 (2012).

[25] S. Chatterjee, P. Dutta, S. Giri, S. Majumdar, S. Sadhukhan, S. Kanungo, S. Chatterjee, M. M. Patidar, G. S. Okram, and V. Ganesan, Glassy magnetic state and negative temperature coefficient of resistivity in Mn^{3+} δ In, Phys. Rev. B **102**, 214443 (2020).

[26] See Supplemental material: This material includes further auxiliary data on structural refinement, transverse resistivity, and computational details, Supplementary URL to be added by journal (2024).

[27] X. Xu, T. Kanomata, M. Hayasaka, R. Umino, K. Endo, H. Nishihara, Y. Adachi, R. Kainuma, and K. A. Ziebeck, Magnetic properties of Mn_2PdSn and Mn_2PdIn, J. Magn. Magn. Mater. **401**, 618–624 (2016).

[28] T. Samanta, P. A. Bhobe, A. Das, A. Kumar, and A. K. Nigam, Reentrant cluster glass and stability of ferromagnetism in the Ga_2MnCo Heusler alloy, Phys. Rev. B **97**, 184421 (2018).

[29] A. K. Nayak, M. Nicklas, S. Chadov, C. Shekhar, Y. Skourski, J. Winterlik, and C. Felser, Large Zero-Field Cooled Exchange-Bias in Bulk Mn_2PtGa, Phys. Rev. Lett. **110**, 127204 (2013).

[30] S. Agarwal, B. Wang, H. Yang, P. Dhanapal, Y. Shen, J. Wang, H. Wang, J. Zhao, and R.-W. Li, Spin-valve-like magnetoresistance in a Ni-Mn-In thin film, Phys. Rev. B **97**, 214427 (2018).

[31] S. Skaftouros, K. Özdoğan, E. ŞaşÄ±oğlu, and I. Galanakis, Generalized Slater-Pauling rule for the inverse Heusler compounds, Phys. Rev. B **87**, 024420 (2013).

[32] M. E. Jamer, Y. J. Wang, G. M. Stephen, I. J. McDonald, A. J. Grutter, G. E. Sterbinsky, D. A. Arena, J. A. Borchers, B. J. Kirby, L. H. Lewis, et al., Compensated ferrimagnetism in the zero-moment Heusler alloy Mn_3Al, Phys. Rev. Appl. **7**, 064036 (2017).

[33] A. K. Nayak, M. Nicklas, S. Chadov, P. Khuntia, C. Shekhar, A. Kalache, M. Baenitz, Y. Skourski, V. K. Guduru, A. Puri, et al., Design of compensated ferrimagnetic Heusler alloys for giant tunable exchange bias, Nat. Mater. **14**, 679–684 (2015).

[34] J. Hessinger and K. Knorr, Field-cooling experiments on the quadrupolar-glass state of $(KBr)_{0.47}(KCN)_{0.53}$, Phys. Rev. Lett. **65**, 2674–2676 (1990).

[35] J. Kroder, K. Manna, D. Kriegner, A. S. Sukhanov, E. Liu, H. Borrmann, A. Hoser, J. Gooth, W. Schnelle, D. S. Inosov, G. H. Fecher, and C. Felser, Spin glass behavior in the disordered half-Heusler compound IrMnGa, Phys. Rev. B **99**, 174410 (2019).

[36] S. Pakhira, C. Mazumdar, R. Ranganathan, S. Giri, and M. Avdeev, Large magnetic cooling power involving frustrated antiferromagnetic spin-glass state in R_2NiSi_3 (R=Gd,Er), Phys. Rev. B **94**, 104414 (2016).

[37] J. C. Phillips, Stretched exponential relaxation in molecular and electronic glasses, Rep. Prog. Phys. **59**, 1133 (1996).

[38] D. Chu, G. G. Kenning, and R. Orbach, Dynamic measurements in a Heisenberg spin glass: CuMn, Phys. Rev. Lett. **72**, 3270–3273 (1994).

[39] J. A. Mydosh, *Spin glasses: An experimental introduction* (CRC Press, 1993).

[40] D. X. Li, S. Nimori, Y. Shiokawa, Y. Haga, E. Yamamoto, and Y. Onuki, ac susceptibility and magnetic relaxation of R_2PdSi_3 ($R = Nd$, Tb, and Dy), Phys. Rev. B **68**, 012413 (2003).

[41] S. Khan, E. S. Y. Aw, L. A. V. Nagle-Cocco, A. Sud, S. Ghosh, M. K. B. Subhan, Z. Xue, C. Freeman, D. Sagkovits, A. GutiÃ©rrez-Llorente, et al., Spin-Glass States Generated in a van der Waals Magnet by Alkali-Ion Intercalation, Adv. Mater. **36**, 2400270 (2024).

[42] J. A. Mydosh, Spin glasses: redux: an updated experimental/materials survey, Rep. Prog. Phys. **78**, 052501 (2015).

[43] P. C. Hohenberg and B. I. Halperin, Theory of dynamic critical phenomena, Rev. Mod. Phys. **49**, 435–479 (1977).

[44] T. Mori and H. Mamiya, Dynamical properties of a crystalline rare-earth boron cluster spin-glass system, Phys. Rev. B **68**, 214422 (2003).

[45] J. Lago, S. J. Blundell, A. Eguia, M. Jansen, and T. Rojo, Three-dimensional Heisenberg spin-glass behavior in $SrFe_{0.90}Co_{0.10}O_{3.0}$, Phys. Rev. B **86**, 064412 (2012).

[46] P. Li, J. Koo, W. Ning, J. Li, L. Miao, L. Min, Y. Zhu, Y. Wang, N. Alem, C.-X. Liu, et al., Giant room temperature anomalous Hall effect and tunable topology in a ferromagnetic topological semimetal Co_2MnAl, Nat. Commun. **11**, 3476 (2020).

[47] A. Rosch, Interplay of Disorder and Spin Fluctuations in the Resistivity near a Quantum Critical Point, Phys. Rev. Lett. **82**, 4280–4283 (1999).

[48] J. A. Mydosh and P. J. Ford, Low temperature electrical resistivity of the spin glass: CuMn, Phys. Lett. A **49**, 189–190 (1974).

[49] I. Belopolski, K. Manna, D. S. Sanchez, G. Chang, B. Ernst, J. Yin, S. S. Zhang, T. Cochran, N. Shumiya, H. Zheng, et al., Discovery of topological Weyl fermion lines and drumhead surface states in a room temperature magnet, Science **365**, 1278–1281 (2019).

[50] C. Hurd, *The Hall effect in metals and alloys* (Springer Science & Business Media, 2012).

[51] R. Karplus and J. M. Luttinger, Hall effect in ferromagnetics, Phys. Rev. **95**, 1154 (1954).

[52] Y. Tian, L. Ye, and X. Jin, Proper Scaling of the Anomalous Hall Effect, Phys. Rev. Lett. **103**, 087206 (2009).

[53] N. Nagaosa, J. Sinova, S. Onoda, A. H. MacDonald, and N. P. Ong, Anomalous Hall effect, Rev. Mod. Phys. **82**, 1539–1592 (2010).

[54] J. P. Perdew, K. Burke, and M. Ernzerhof, Generalized gradient approximation made simple, Phys. Rev. Lett. **77**, 3865 (1996).

[55] P. E. BlÃ¶chl, Projector augmented-wave method, Phys. Rev. B **50**, 17953 (1994).

[56] Q. Wu, S. Zhang, H.-F. Song, M. Troyer, and A. A. Soluyanov, WannierTools: An open-source software package for novel topological materials, Comput. Phys. Commun. **224**, 405–416 (2018).

[57] G. Pizzi, V. Vitale, R. Arita, S. BlÃ¼gel, F. Freimuth, G. GÃ©ranton, M. Gibertini, D. Gresch, C. Johnson, T. Koretsune, et al., Wannier90 as a community code: new features and applications, J. Phys.: Condens. Matter **32**,

165902 (2020).
[58] M. G. Lopez, D. Vanderbilt, T. Thonhauser, and I. Souza, Wannier-based calculation of the orbital magnetization in crystals, Phys. Rev. B **85**, 014435 (2012).
[59] M. I. Aroyo, J. M. Perez-Mato, D. Orobengoa, E. Tasci, G. De La Flor, and A. Kirov, Crystallography online: Bilbao crystallographic server, Bulg. Chem. Commun. **43**, 183-197 (2011).
[60] X. Wang, J. R. Yates, I. Souza, and D. Vanderbilt, Ab initio calculation of the anomalous Hall conductivity by Wannier interpolation, Phys. Rev. B **74**, 195118 (2006).
[61] H. T. Stokes, D. M. Hatch, and B. J. Campbell, FINDSYM, ISOTROPY Software Suite, iso.byu.edu.
[62] D. M. Hatch and H. T. Stokes, FINDSYM: program for identifying the space-group symmetry of a crystal, J. Appl. Crystallogr. **38**, 237-238 (2005).
[63] M. Park, G. Han, and S. H. Rhim, Anomalous Hall effect in a compensated ferrimagnet: Symmetry analysis for Mn_3Al, Phys. Rev. Res. **4**, 013215 (2022).
[64] G. Gurung, D. F. Shao, T. R. Paudel, and E. Y. Tsymbal, Anomalous Hall conductivity of noncollinear magnetic antiperovskites, Phys. Rev. Mater. **3**, 044409 (2019).
[65] J. Zhou, X. Shu, Y. Liu, X. Wang, W. Lin, S. Chen, L. Liu, Q. Xie, T. Hong, P. Yang, B. Yan, X. Han, and J. Chen, Magnetic asymmetry induced anomalous spin-orbit torque in IrMn, Phys. Rev. B **101**, 184403 (2020).
[66] X. Wang, D. Vanderbilt, J. R. Yates, and I. Souza, Fermi-surface calculation of the anomalous Hall conductivity, Phys. Rev. B **76**, 195109 (2007).
[67] Y. Yao, L. Kleinman, A. H. MacDonald, J. Sinova, T. Jungwirth, D.-S. Wang, E. Wang, and Q. Niu, First principles calculation of anomalous Hall conductivity in ferromagnetic bcc Fe, Phys. Rev. Lett. **92**, 037204 (2004).
[68] J. Shen, Q. Yao, Q. Zeng, H. Sun, X. Xi, G. Wu, W. Wang, B. Shen, Q. Liu, and E. Liu, Local Disorder-Induced Elevation of Intrinsic Anomalous Hall Conductance in an Electron-Doped Magnetic Weyl Semimetal, Phys. Rev. Lett. **125**, 086602 (2020).
[69] G. Kresse, and J. Hafner, Ab initio molecular dynamics for liquid metals, Phys. Rev. B **47**, 558-561 (1993).
[70] G. Kresse, and D. Joubert, From ultrasoft pseudopotentials to the projector augmented-wave method, Phys. Rev. B **59**, 1758-1775 (1999).
[71] H.J. Monkhorst, and J.D. Pack, Special points for Brillouin-zone integrations, Phys. Rev. B **13**, 5188-5192 (1976).
[72] J.P. Perdew, K. Burke, and M. Ernzerhof, Generalized gradient approximation made simple, Phys. Rev. Lett. **77**, 3865-3868 (1996).
[73] P. Singh, M.K. Harbola, M. Hemanadhan, A. Mookerjee, and D.D. Johnson, Better band gaps with asymptotically corrected local exchange potentials, Phys. Rev. B **93**, 085204 (2016).
[74] P. Singh, M.K. Harbola, B. Sanyal, and A. Mookerjee, Accurate determination of band gaps within density functional formalism, Phys. Rev. B **87**, 235110 (2013).
[75] T. Kaneyoshi, Sing glass ordering temperature beyond its mean-field, Journal of Magnetism and Magnetic Materials **15-18**, 119-120 (1980).
[76] M. R. A. Shegelski and D. J. W. Geldart, Theory of freezing temperatures of metallic spin glasses, Solid State Commun. **79**, 769 (1991).
[77] M. R. A. Shegelski and D. J. W. Geldart, Indirect-exchange interactions in disordered metals at finite temperature, Phys. Rev. B **46**, 5318 (1992).
[78] M. R. A. Shegelski and D. J. W. Geldart, Theory of impurity-concentration dependence of freezing temperatures of metallic spin glasses, Phys. Rev. B **46**, 2853 (1992).
[79] Y. Yao, L. Kleinman, A. H. MacDonald, J. Sinova, T. Jungwirth, D.-S. Wang, E. Wang, and Q. Niu, First Principles Calculation of Anomalous Hall Conductivity in Ferromagnetic bcc Fe, Phys. Rev. Lett. **92**, 037204 (2004).
[80] H.-R. Fuh and G.-Y. Guo, Intrinsic anomalous Hall effect in nickel: A GGA+U study, Phys. Rev. B **84**, 144427 (2011).
[81] H.-L. Huang et al., Anomalous Hall effect and current spin polarization in Co2FeX Heusler compounds (X = Al, Ga, In, Si, Ge, and Sn): A systematic ab initio study, Phys. Rev. B **91**, 134409 (2015).
[82] G. Y. Guo, Q. Niu, and N. Nagaosa, Anomalous Nernst and Hall effects in magnetized platinum and palladium, Phys. Rev B **89**, 214406 (2014).
[83] J. Kübler, and C. Felser, Berry curvature and the anomalous Hall effect in Heusler compounds, Phys. Rev. B **85**, 012405 (2012).
[84] J. Kudrnovsky, V. Drchal, and I. Turek, Anomalous Hall effect in stoichiometric Heusler alloys with native disorder: A first-principles study, Phys. Rev. B **88**, 014422 (2013)
[85] J. C. Tung, and G. Y. Guo, High spin polarization of the anomalous Hall current in Co-based Heusler compounds, New J. Phys. **15**, 033014 (2013).
[86] J. Noky, Y. Zhang, J. Gooth et al. Giant anomalous Hall and Nernst effect in magnetic cubic Heusler compounds, npj Comput Mater **6**, 77 (2020).
[87] S. Chadov, X. Qi, J. Kübler et al. Tunable multifunctional topological insulators in ternary Heusler compounds, Nature Mater **9**, 541-545 (2010).
[88] A. Ahmed, A. Bhattacharya, and I. Das, Anomalous and large topological Hall effects in β-Mn chiral compound $Co_{6.5}Ru_{1.5}Zn_8Mn_4$: electron-electron interaction facilitated quantum interference effect, *J. Phys.: Condens. Matter* **37**, 115802 (2025).